



Franken, J. H., van der Heijden, M. A.J., Ellis, T. H., Lavrijsen, R. , Daniels , C., McGrouther, D., Swagten , H. J.M., and Koopmans, B.(2014) *Beam-induced Fe nanopillars as tunable domain-wall pinning sites*. *Advanced Functional Materials*, 24 (23). pp. 3508-3514. ISSN 1616-301X

Copyright © 2014 WILEY-VCH Verlag GmbH & Co. KGaA, Weinheim

A copy can be downloaded for personal non-commercial research or study, without prior permission or charge

Content must not be changed in any way or reproduced in any format or medium without the formal permission of the copyright holder(s)

When referring to this work, full bibliographic details must be given

<http://eprints.gla.ac.uk/94312/>

Deposited on: 10 November 2014

Enlighten – Research publications by members of the University of Glasgow
<http://eprints.gla.ac.uk>

Franken, Jeroen H., van der Heijden, Mark A. J., Ellis, Tim H., Lavrijsen, Reinoud , Daniels , Carsten, McGrouther, Damien, Swagten , Henk J. M., and Koopmans, Bert (2014) *Beam-induced Fe nanopillars as tunable domain-wall pinning sites*. *Advanced Functional Materials* . ISSN 1616-301X

Copyright © 2014 WILEY-VCH Verlag GmbH & Co. KGaA, Weinheim

A copy can be downloaded for personal non-commercial research or study, without prior permission or charge

Content must not be changed in any way or reproduced in any format or medium without the formal permission of the copyright holder(s)

When referring to this work, full bibliographic details must be given

<http://eprints.gla.ac.uk/94312/>

Deposited on: 9 June 2014

DOI: 10.1002/ adfm.xxx

Article type: Full paper

Beam-induced Fe nanopillars as tunable domain-wall pinning sites

By *Jeroen Franken, Mark van der Heijden, Tim Ellis, Reinoud Lavrijsen, Carsten Daniels, Damien McGrouther, Henk Swagten**, and *Bert Koopmans*

[*] Prof. H. J. M. Swagten, J. H. Franken, M. A. J. van der Heijden, T. H. Ellis, Dr. R. Lavrijsen, C. Daniels, Prof. B. Koopmans
Department of Applied Physics, Center for NanoMaterials,
Eindhoven University of Technology,
P.O. Box 513, 5600 MB Eindhoven (Netherlands)
E-mail: H.J.M.Swagten@tue.nl

Dr. D. McGrouther, C. Daniels
SUPA, School of Physics and Astronomy,
University of Glasgow,
G12 8QQ (United Kingdom)

Keywords: beam induced deposition, magnetic nanostructures, magnetic domain walls, transmission electron microscopy, nanosensors

We employ Focused-Electron-Beam-Induced Deposition (FEBID) to create freestanding magnetic nanostructures. By growing Fe nanopillars on top of a perpendicular magnetic domain wall (DW) conduit, pinning of the DWs is observed due to the stray fields emanating from the nanopillar. Furthermore, we observe a different DW pinning behavior between the up and down magnetic states of the pillar, allowing us to deduce the switching fields of the pillar in a novel way. The implications of these results are twofold: not only can 3-dimensional nano-objects be used to control DW motion in applications, we also propose that DW motion is a unique tool to probe the magnetic properties of nano-objects.

1. Introduction

Magnetic domain walls (DWs) receive widespread attention due to their promising application in novel nanodevices^[1-3]. In an envisioned 3-dimensional memory device, DWs are propagated between discrete sites along a nanostrip, forming a bit shift register with a very high data density^[1]. However, an efficient way to pin DWs at discrete positions is needed^[4], and novel nanostructuring techniques are required to create 3-dimensional structures. An interesting new route to 3-dimensional nanostructures is provided by Focused-Electron-Beam-Induced Deposition (FEBID)^[5-16], a tool that can be used to create nano-objects of any desired shape. Here, we employ this technique to create vertical iron nanopillars and demonstrate their magnetic behavior through the effect they have on DW motion in an underlying DW conduit. We show that the stray fields from a magnetic nanopillar serve as an efficient pinning site for a magnetic DW **in materials with perpendicular magnetic anisotropy (PMA)**, and that the pinning can be tuned by the height of the pillar as well as its magnetic state. This proves that these small freestanding structures are indeed magnetic, which we also show unambiguously by imaging the stray fields of the pillars in a Lorentz Transmission Electron Microscope (TEM). Furthermore, we exploit the fact that DW pinning depends on the magnetic state of the pillar, to determine the switching field of the pillars themselves. **This way** of probing magnetic nano-objects is potentially interesting for nanomagnetic sensors based on domain-walls^[17-20].

2. Imaging stray fields of magnetic pillars

To perform the experiments, pillars with diameters between 45 and 70 nm were grown using an Fe₂(CO)₉ precursor^[21,22] and a focused electron beam (see Methods section). This yielded pillars with at most 60% Fe, with O and C as the other main constituents^[21]. By changing the dwell time and precursor pressure, the height of the pillars is varied between 100 nm and 1 μm. First, we confirm the properties and magnetic behavior of the pillars by direct imaging

using a (Scanning) Transmission Electron Microscope ((S)TEM) equipped with a cold field emission gun. **Fig. 1(a)** shows a high magnification dark field image of one of the pillars. It can be seen that the width of the pillar is ~ 53 nm and it consists of an amorphous/ultra nano-crystalline core surrounded by a poly-crystalline coating, 6 nm in thickness, which has been previously shown^[21] to be Fe_3O_4 . The radius of curvature at the tip of the pillar is ~ 20 nm.

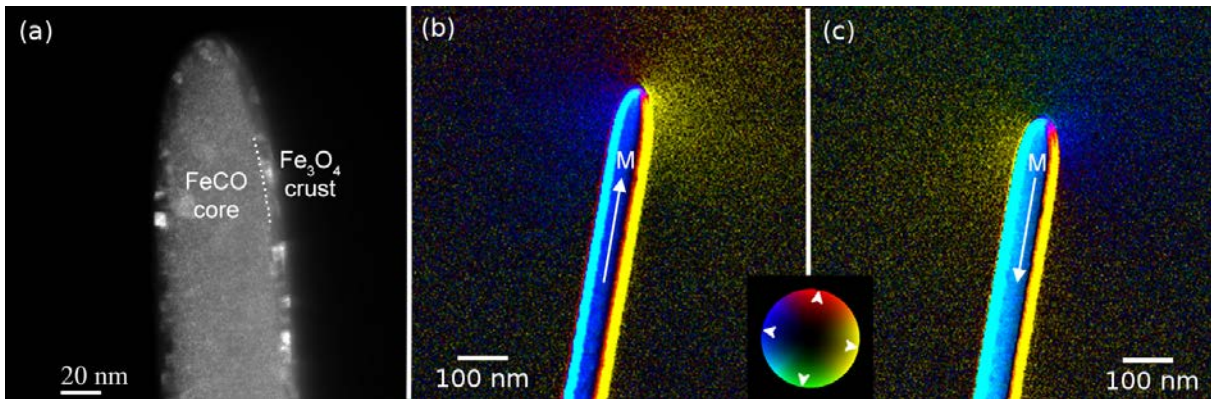


Figure 1. (a) Dark field TEM image showing the pillar geometry and structure. (b) & (c) color DPC mode STEM images showing stray fields emanating from the pillar tip. From (b) to (c), the stray field directions **in the space** around the tip are inverted (see color code) when the magnetization of the pillar is switched by means of an external field (53 mT). **The color contrast in the pillar itself is non-interpretable (see main text).**

Fig. 1(b) and 1(c) show color Differential Phase Contrast (DPC) images^[23,24] of a 1.2 μm high pillar, acquired from operation of the microscope in Lorentz STEM mode (see Methods section). In both figures, in the free-space adjacent to the top of the pillars, color contrast is observed that relates to the stray fields emanating from the pillar. The color contrast in the pillar itself is unfortunately non-interpretable, because it is dominated by strong electrostatic contributions arising due to the circular cross-section and oxide layer that obscure the magnetic component. In Fig. 1(b), moving clockwise around the pillar tip, the color contrast changes from blue to red to yellow. By referring to the color wheel, the magnetostatic fields can be understood to be diverging from the tip. That no strong magnetostatic contrast is observed anywhere else but at the base of the pillar suggests strongly that it is uniformly

magnetized in an upwards direction (any DWs within such narrow pillars would be expected to have associated stray field distributions). After application of a magnetic field of 53 mT oriented downwards, the magnetostatic color contrast at the tip in Fig. 1(c) is observed to have altered. Moving round the tip in a clockwise direction, the colors go from yellow to green to blue, from which it is inferred that the magnetization in the pillar has been reversed by the field.

3. Stray-field induced pinning

We now study the effect that the stray fields emanating from the base of the pillar have on domain wall motion in underlying DW conduits. It has previously been shown that dipolar stray fields generated by an array of nanodots produced by a conventional lithography method alters the average speed of DW motion in a 2-dimensional film ^[25], but here our aim is to completely stop a DW in a 1-dimensional DW conduit by a single nanopillar of varying height. An analogous approach was studied in detail in systems where the magnetization was oriented along the length of the DW conduit, by the use of dipolar fields generated by coplanar magnetic nanobars ^[26–28] or by a small coil wound around a microwire ^[29]. The reciprocal effect was also studied, where the stray field of a moving DW was used to assist switching of a nearby magnetic element ^[30]. However, inducing DW pinning by stray fields that are oriented in-plane seems less appropriate in materials with perpendicular magnetization which are studied here. Although it could work to some extent because the magnetization inside the DW is also oriented in-plane, the pinning effect is expected to be small given the very small DW width that these materials typically exhibit, yielding a low interaction energy. Instead, an approach using perpendicularly oriented stray fields seems more appropriate, and such a field could be provided by our vertical nanopillars grown on top of a DW conduit.

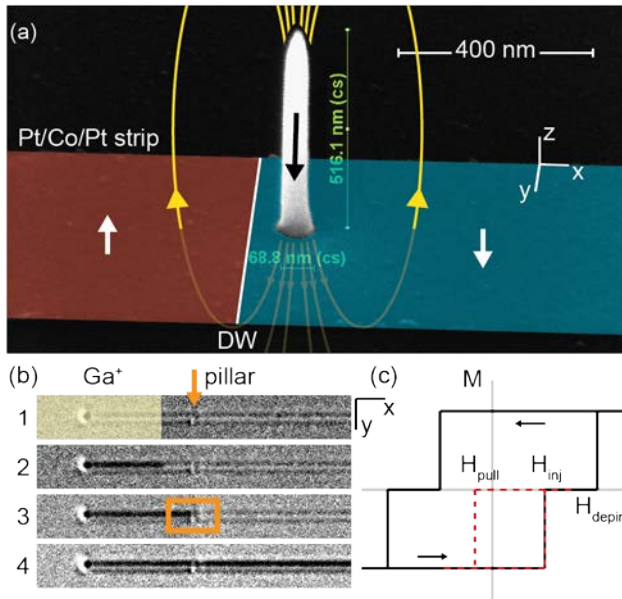


Figure 2. (a) SEM micrograph of a Fe nanopillar deposited on top of a Pt/Co/Pt strip. A DW, present at the transition between up (red) and down (blue) magnetization, pins in front of the pillar because the domains are aligned with the pillar stray field (yellow field lines) in that case. (b) Kerr microscopy snapshots of the DW pinning experiment on a Pt/Co/Pt strip. The left (yellow) area of the strip is irradiated with Ga irradiation to nucleate a DW at low field. After negative saturation (1), the field is increased until the irradiated area is switched at ~ 2 mT (2), the DW depins from the irradiation boundary at $H_{inj} \approx 3$ mT and subsequently pins at the pillar (3), and finally the DW depins from the pillar at H_{depin} (4). A schematic hysteresis loop averaged over the (orange) region of interest is sketched in figure (c). A minor loop (red dashed line), is used to identify the negative field needed to move the DW back from the pillar position (H_{pull}).

The DW conduits consist of 500 nm wide Pt/Co/Pt strips, fabricated by electron beam lithography, sputtering and lift-off. This material exhibits PMA, so the magnetization is perpendicular to the sample plane in the two domains (up and down) which are separated by a DW as indicated in Fig. 2(a). In order to introduce a DW into the conduit at a low and controlled magnetic field, Ga^+ irradiation with a focused ion beam is employed on an area to the left of the pillar as indicated in Figure 2(b) (bright yellow area) to locally reduce the DW creation field^[31]. The FIB was put slightly out of focus to get a smoother irradiation boundary, thereby reducing DW pinning at the boundary^[32,33] and making it easier to inject a DW into the non-irradiated part of the DW conduit, where our pillar is located. The field required to inject a DW into the conduit such that it can freely move towards the pillar is defined as the

injection field H_{inj} and has a typical value of 3 mT. For an untreated microwire, the injection field would be much higher at typically 23 mT, and the domain wall would originate from an uncontrolled position.

Switching of the strips was studied using Kerr microscopy, and snapshots of the magnetic state of the DW conduit with increasing magnetic field are shown in Fig. 2(b). The first image shows the saturated single-domain state at zero field, after coming from a high negative perpendicular field (-100 mT). As we will show later, both the pillar and the DW conduit are magnetized downwards in this starting position. While increasing the field, the second image shows nucleation of a domain wall in the irradiated area of the conduit (black and white contrast), which pins at the irradiation boundary. Further increasing the field in the third image, this domain wall is injected into the DW conduit but, remarkably, stops at the position where our pillar is located. This shows that FEBID-grown Fe pillars can indeed be used to pin a DW and since the effect is absent with non-magnetic Pt pillars (not shown), the pinning potential has to originate from the stray fields induced by the magnetic pillar. The last image shows that the DW can be depinned from the pillar if a sufficiently high field is applied. By averaging the optical contrast of the area around the pillar as a function of field (see Fig. 2(b)(3), orange rectangle), a hysteresis loop can be obtained as sketched in Fig. 2(c) (black line), where the plateau between H_{inj} and H_{depin} indicates DW pinning. The field strength at which the DW leaves the pillar position is defined as the depinning field H_{depin} .

While we have shown that the pillar can block the motion of the DW in the forward direction, one could wonder if the same applies to the backward direction. Therefore, we also try pulling a DW that is pinned at the pillar position back to the direction where it came from, by sweeping back the field when the plateau is reached (minor loop in Fig. 2(c)). It was found that this ‘pulling field’ $|H_{pull}|$ required to move the DW to the left side was consistently lower than the depinning field $|H_{depin}|$ required to move it to the right, and also lower than the

injection field $|H_{inj}|$ required to inject a new (opposite) DW from the left side. This is

compatible with a picture of DW pinning by the magnetic stray fields emanating from a pillar with fixed magnetization as shown in Fig. 2(a). This creates a favorable position for the DW right in front of the pillar where there is a transition of the z-component of the stray field from up to down, to align with the magnetization in the two domains. A significantly higher field is required to overcome the strong z-field right underneath the pillar and move the DW forward, as compared to the field needed to pull the DW back to overcome the weak opposite stray field in front of the pillar^[25].

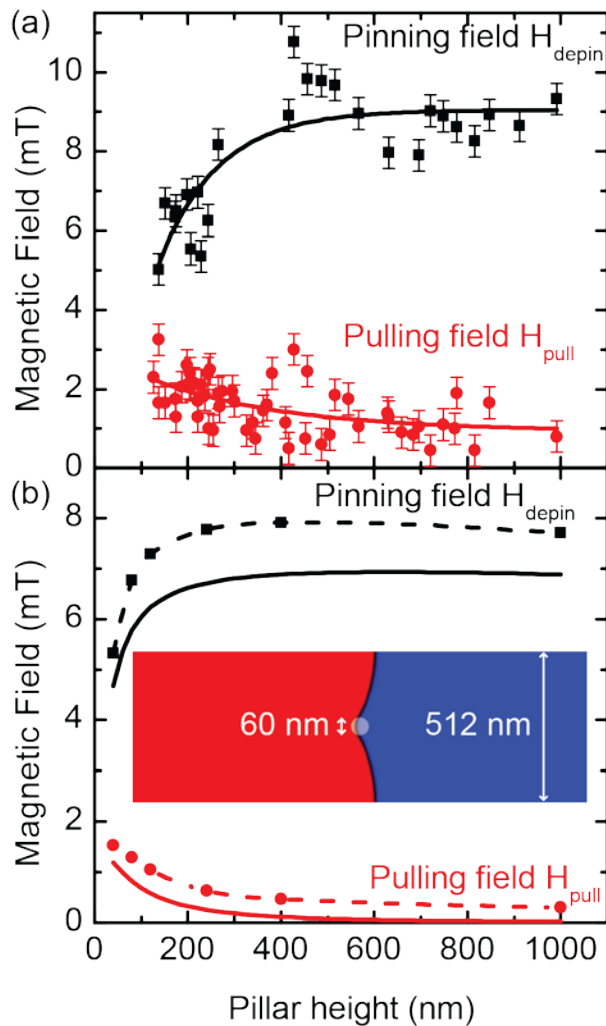


Figure 3. (a) Measured pinning (black squares) and pulling fields (red circles) as a function of pillar height. The lines are to guide the eye. (b) (solid lines) Pinning and pulling field expected based on a 1D DW model. The behavior is confirmed by full micromagnetic simulations (squares and circles). The simulation snapshot in the inset show that the DW deviates from a 1D description by bending around the pillar (white circle) before depinning.

To find further proof for the pinning mechanism based on stray fields, we explore the tunability of the pinning effect by varying the pillar height as shown in **Fig. 3(a)**. The pillar height determines the stray-field-induced DW potential landscape underneath the pillars; a higher pillar gives a higher stray field right underneath the pillar, whereas field lines become more dispersed away from the pillar yielding a smaller opposite stray field in the circumference (see Supporting Information). This is clearly observed in the magnitude of both the pinning and pulling field; the **depinning** field (a measure for the stray fields underneath the pillar) clearly increases with pillar height, whereas the pulling field appears to decrease slightly.

We now turn to a simple model to explain the DW pinning, based on the stray field that a pillar induces in the plane of the DW conduit (2 nm below the pillar). The stray field calculation was done as a function of pillar height using the Biot-Savart law, assuming a homogeneously magnetized cylinder with a diameter of 60 nm (see Supporting Information for details). This was used as input for a 1-dimensional (1D) DW model, where it was assumed that a DW at position x along the strip senses the z -component of the stray field, averaged along the width of the strip (500 nm). The calculated pinning and pulling fields reproduce the observed experimental behavior (Fig. 3(b)). The **depinning** field increases for higher pillars (solid black line), whereas the pulling field is much lower and decreases (solid red line). In fact, we can use the measured DW pinning strength as a magnetometer for the pillar's magnetization, by choosing a value of M_s that gives agreement between model and experiment. A good match is found for $M_s \approx 100$ kA/m, and this value was used in the calculation of Fig. 3(b). This deduced value of M_s is much lower than for pure Fe (1700 kA/m), which can be due to various reasons. First of all, the Fe content is much lower than 100%. In planar non-freestanding depositions grown in the same vacuum, a Fe content of

60% percent was found using Energy-dispersive X-ray spectroscopy (EDX)^[21], but this does not necessarily translate to the pillar geometry, since the pillar has a relatively large surface area which is sensitive to oxidation, and the temperature during growth is expectedly different. We therefore might expect less than 60% Fe in the pillars. Secondly, the value of M_s is likely underestimated due to the effect of thermal activation: at room temperature, random fluctuations can lead to an escape of the DW over a finite energy barrier, which reduces the pinning field as compared to our zero-temperature model^[26]. Thirdly, M_s may be underestimated if the remanence is less than 100%. Fourthly, other complicating factors are the precise shape of the bottom of the pillar, or the possibility of a compositional gradient along the length of the pillar. In Fe pillars grown by different precursor gases^[9,14,15], remnant magnetizations in the range 160 – 600 kA/m were found by Electron Holography TEM^[15], so our result is at the lower end of this range. This is however beneficial for our experiment, since we observed in the simulations that a higher magnetization could lead to nucleation of a new domain rather than pinning of an existing DW in the conduit.

To confirm that our simplified 1D-model gives a reasonable estimate of the pinning potential, full 2D micromagnetic calculations of a DW moving underneath a pillar are also conducted^[34]. The calculated pillar stray field maps are used as a position-dependent external field acting on a 512 nm wide, 0.5 nm thick strip with perpendicular magnetization. The strip has a saturation magnetization $M_s = 1400$ kA/m, uniaxial anisotropy constant $K_u = 1.5$ MJ/m³, and exchange constant 16 pJ/m^[33]. The magnetization of the pillar is assumed to remain fixed in the $-z$ direction. Starting from an artificially created DW on the left side of the pillar, we study how the DW moves to the right while increasing the applied field in small steps. The field at which the DW detaches from the pillar and moves out on the right of the strip is defined as the depinning field. Interestingly, it is observed that the DW does not retain a 1D profile but bends around the pillar because of the high stray fields underneath it (inset of Fig.

3(b)). This, combined with additional contributions from the in-plane components of the stray field, leads to **depinning** fields that are slightly different but comparable in magnitude to the 1D-model. Repeating the simulations with varying pillar height reproduces the trend of increasing **depinning** field with increasing height (black squares in Fig. 3(b)). The pulling field was also simulated by sweeping the field in the negative direction in order to move the DW to the left, and again the 1D-model trend was reproduced (red circles in Fig. 3(b)).

4. Probing the coercive field of pillars

So far, it was assumed that the magnetization in the pillar remains fixed during the experiment. However, if the pillar itself switches with respect to the magnetization of the strip, the pinning behavior should also invert. In fact, this provides us with a unique tool to determine the magnetic state of the pillar. We exploit this to deduce the coercive field (or switching field) of the pillar from the DW pinning characteristics. Like before, we measure hysteresis loops in the region of interest around the pillar starting from high negative saturation, but this time we vary the **maximum positive** field H_{\max} in each recorded loop, as seen in **Fig. 4(a)**. It is seen that there are two possible shapes of the hysteresis loop. The cartoons in Fig. 3(a) schematically show what happens in the two cases. In case (I), H_{\max} is higher than the coercive field of the pillar, so that the forward and backward sweep are completely symmetric. In that case, we start from a saturated state in both the forward and backward sweep of the loop (the top and middle row of cartoons, respectively), and observe the features of DW nucleation, DW pinning and DW depinning on both sides of the loop. In case (II) however, H_{\max} is **lower than the coercive field of the pillar, such** that the pillar is not switched during the forward sweep, and the magnetization of the pillar and the DW conduit are not aligned when the backward sweep is started (bottom left cartoon in Fig. 4(a)). The new domain that is nucleated in the next cartoon, is now aligned with the pillar's

magnetization and therefore easily moves underneath the pillar once it reaches it. The DW might experience the (much smaller) pulling field when it leaves the pillar on the right side, but this is not observable in the experiment since the pulling field is much lower than the injection field that was needed to bring the DW to the pillar in the first place. Therefore, no plateau is observed in the hysteresis loop during the backward sweep in case (II), which makes it possible to distinguish whether the pillar was switched or not.

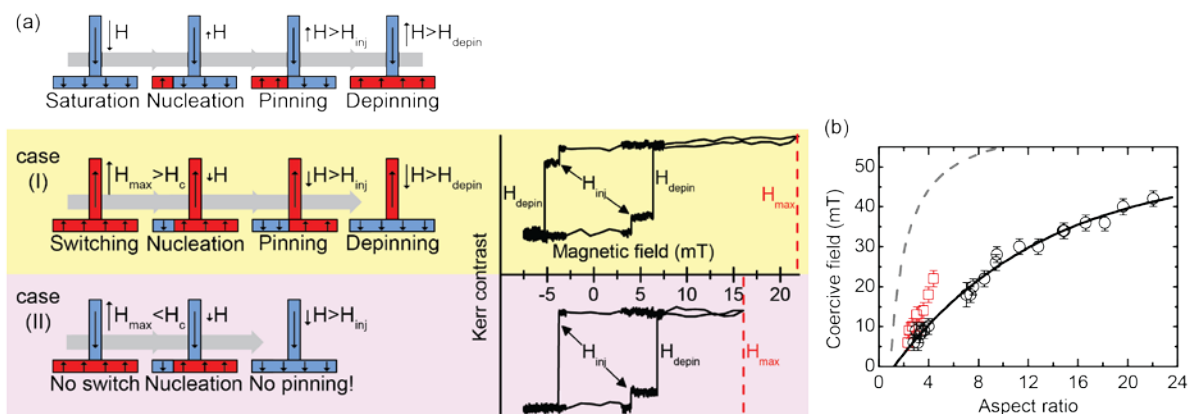


Figure 4. (a) (right) Hysteresis loops as a function of **maximum positive** field H_{max} ; depending on H_{max} , the pillar either switches or does not switch, leading to symmetric (case I) or asymmetric (case II) hysteresis loops. This difference is explained by the cartoons on the left. (b) Coercive field as a function of pillar aspect ratio. The solid line is a guide to the eye. The red data points are outside of the trend because these pillars were grown under slightly different circumstances. The dashed grey line represents the coercive field of pillars based on the Stoner-Wohlfarth model.

The coercive fields are thus obtained simply by repeating the hysteresis loops at increasing H_{max} until symmetric (case I) behavior is observed. The results are plotted as a function of pillar aspect ratio (height divided by diameter) in Fig. 4(b) (black circles). It is observed that at increasing pillar aspect ratio (height), the coercive field increases. This is qualitatively compatible with the coercive fields of magnetic cylinders calculated with the Stoner Wohlfarth model^[35,36] **assuming $M_s=100$ kA/m like before** (dashed grey line in Fig. 4(b), see Supporting Information for calculation details). However, the coercive field saturates already at lower pillar aspect ratios in the model, compared to the experimental data. This implies that the Stoner-Wohlfarth model, which assumes a single domain structure of the pillar, probably

represents a too simplified description, and switching mechanisms involving nonuniform magnetization might play a role^[16,21,37]. This microscopic switching mechanism cannot be revealed with our measurement scheme and is therefore beyond the scope of this paper. In fact, we are mostly sensitive to the magnetization in the bottom part of the pillar, hence it cannot be guaranteed that the whole pillar switches together. In that case the data represents only the switching field of the bottom part, which might be different from the rest of the pillar. Finally, we would like to show that the switching field is strongly influenced by compositional variations. The red square data points in Fig. 4(b) are representing pillars grown in the same vacuum but in a later run, where the precursor pressure had dropped leading to a lower growth rate. This also has an influence on the composition and this is reflected in a different coercive field compared to similarly high pillars grown at a higher pressure (red squares).

5. Conclusion

In conclusion, we have shown by both TEM and optical Kerr microscopy that FEBID-grown Fe nanopillars are magnetic and can be used to pin DWs in a PMA strip, where the pinning strength is tuned by the pillar height. The observed DW pinning was explained using a simplified 1D-model and supported by full micromagnetic simulations. By comparing simulations and experiment, the DW pinning process can in principle be used as a magnetometer for the pillar's magnetization, and a value $M_s=100$ kA/m was found as a rough estimate. Furthermore, we exploited the fact that DW pinning depends on the magnetic orientation of the pillar, allowing us to determine the coercive fields of such nanopillars. The observed coercive field increases with the pillar aspect ratio, which was qualitatively explained with a Stoner-Wohlfarth model. The use of DW motion as a probe of nanomagnetic objects is potentially interesting for use in sensors or lab-on-chip applications^[38-42], as an alternative to more conventional magnetoresistive sensors^[38,39] or anomalous Hall effect

sensors^[43]. We already mentioned previous studies demonstrating sensitivity of in-plane magnetized DW conduits to external ferromagnetic objects^[26-28], and similar conduits were also shown to be sensitive to the presence of magnetic beads^[17-20] used as markers in biosensors. Here, we applied such phenomena to technologically relevant PMA materials. As an example, one could devise an instrument that measures the absence, presence, magnetic moment, size or switch field of a single magnetic nano-object which lies on a DW conduit, by measuring the field that is required to move the DW past the object to a read-out position. As recognized by Vavassori et al.^[17], the key fundamental advantage of using a DW for sensor purposes is the fact that the sensing area is determined by the DW width, which happens to be especially small in PMA materials (~10 nm). Another advantage of a DW sensor is its high mobility, meaning that the position of the probed object does not matter as long as it is somewhere on the DW conduit. However, drawbacks are the fact that there usually occurs random pinning in the DW conduit of the order of 1 mT, which masks stray-field-induced pinning below this value, and the measurement scheme in its current form is rather complex. Looking at applications of the pillars themselves, they could be used to selectively pin DWs of a certain polarity. This feature makes them less suitable for application in a current-driven DW shift register^[1], where pinning sites should act equally on up-down and down-up domain walls, but could be employed as a polarity filter in other applications such as DW logic. Since external magnetic objects such as our pillars do not appreciably alter the DW properties in the underlying DW conduit, they can be beneficial compared to pinning sites that are structured in the DW conduit itself^[26,28]. Furthermore, the pillars' functionality can be reprogrammed by switching their magnetic state, enabling the fabrication of versatile magnetic logic devices.

6. Methods

Sample fabrication: The Pt/Co/Pt domain wall conduits were produced on Si/SiO₂ (100nm) substrates by E-beam lithography using PMMA as resist, developed in MIBK, sputtered at an Ar pressure of $\sim 10^{-2}$ mbar (base pressure 3×10^{-8} mbar), followed by lift-off in acetone. On top of these conduits, the Fe pillars were grown in a dual-beam system (FEI Nova 600i NanoLab) at a precursor pressure between 2.06 and 4.12×10^{-6} mbar, using a focused electron beam operating at 5kV and 0.4 nA. The pillar height was controlled by changing the dwell time between 10 and 30 s. Since the precursor pressure decreases during a deposition run, the exact height cannot be controlled accurately; therefore we measure the width and height of each individual pillar afterwards using SEM images. Dividing height by width gives the aspect ratio of a pillar. The pillars that were studied in the TEM microscope (JEOL ARM200FCS) were grown on an Omniprobe Cu Lift-Out grid under similar circumstances.

Stray field imaging:

The magnetic contrast in Fig. 1(b) and 1(c) was obtained using a custom Scanning Transmission Electron Microscopy (STEM) mode known as Differential Phase Contrast (DPC) imaging. Contrast arising from phase shifts of the electron beam wave-function, from both electrostatic and magnetic origins, is detected via the Lorentz deflection caused to the electron beam. The angle of the deflection, typically $< 50 \mu\text{rad}$, is measured by use of a segmented photo-diode detector with an arrangement consisting of an inner solid quadrant and an outer annular quadrant. The DPC images shown here can be understood by simply considering the post-specimen beam to impinge upon the solid inner quadrant. Deflections of the electron beam result in it being moved off of the center of the detector. Obtaining difference images, by subtracting the image signals detected from opposite quadrants when scanning, leads to grayscale phase contrast images that are proportional to the components of the beam deflection along orthogonal directions of sensitivity. These grayscale component images are then combined to produce a color vector representation of the phase contrast ^[23].

Kerr microscopy: Before recording the Kerr microscopy snapshots of the DW conduits in Fig. 2(b), the sample was saturated in negative field and a background image was recorded at zero field. This background image has been subtracted to produce all shown subsequent images, so that only changes in the magnetization with respect to the saturated state are visible. The border that is seen around the Pt/Co/Pt strip is because of a slight drift of the sample after the background was recorded. The field is increased in small steps of 0.02 mT and the magnetic state is recorded after each step. This leads to an effective field sweep rate of approximately 0.1 mT/s limited by the acquisition time of the CCD camera. The magnetic contrast that is observed is only due to the DW conduit, since the MOKE signal from the vertical pillars is negligible.

Acknowledgements

This work is part of the research programme of the Foundation for Fundamental Research on Matter (FOM), which is part of the Netherlands Organisation for Scientific Research (NWO). We thank NanoNed, a Dutch nanotechnology program of the Ministry of Economic Affairs. DMG and CD wish to acknowledge technical support provided by C. How and S. MacFadzean. JHF, MAJH, TE, RL, HJMS and BK wish to acknowledge technical support provided by B. Barcones.

Received: ((will be filled in by the editorial staff))

Revised: ((will be filled in by the editorial staff))

Published online: ((will be filled in by the editorial staff))

References

- [1] S. S. P. Parkin, M. Hayashi, L. Thomas, *Science* **2008**, *320*, 190.
- [2] D. A. Allwood, G. Xiong, C. C. Faulkner, D. Atkinson, D. Petit, R. P. Cowburn, *Science* **2005**, *309*, 1688.
- [3] J. H. Franken, H. J. M. Swagten, B. Koopmans, *Nat. Nanotech.* **2012**, *7*, 499.
- [4] X. Jiang, L. Thomas, R. Moriya, S. S. P. Parkin, *Nano Lett.* **2011**, *11*, 96.
- [5] W. F. van Dorp, C. W. Hagen, *J. Appl. Phys.* **2008**, *104*, 081301.
- [6] R. R. Kunz, T. M. Mayer, *Appl. Phys. Lett.* **1987**, *50*, 962.
- [7] M. A. Bruk, E. N. Zhikharev, E. I. Grigor'ev, A. V. Spirin, V. A. Kal'nov, I. E. Kardash, *High Energy Chem.* **2005**, *39*, 65.
- [8] W. Zhang, M. Shimojo, M. Takeguchi, R.-C. Che, K. Furuya, *Adv. Eng. Mater.* **2006**, *8*, 711.
- [9] M. Takeguchi, M. Shimojo, K. Furuya, *Nanotechnology* **2005**, *16*, 1321.
- [10] A. Fernández-Pacheco, J. M. De Teresa, R. Córdoba, M. R. Ibarra, D. Petit, D. E. Read, L. O'Brien, E. R. Lewis, H. T. Zeng, R. P. Cowburn, *Appl. Phys. Lett.* **2009**, *94*, 192509.
- [11] I. Utke, P. Hoffmann, J. Melngailis, *J. Vac. Sci. Technol. B* **2008**, *26*, 1197.
- [12] W. F. van Dorp, B. van Someren, C. W. Hagen, P. Kruit, P. A. Crozier, *Nano Lett.* **2005**, *5*, 1303.
- [13] M. Gavagnin, H. D. Wanzenboeck, D. Belić, E. Bertagnolli, *ACS Nano* **2013**, *7*, 777.
- [14] M. Takeguchi, M. Shimojo, R. Che, K. Furuya, *J. Mater. Sci.* **2006**, *41*, 2627.
- [15] M. Takeguchi, M. Shimojo, K. Mitsuishi, M. Tanaka, R. Che, K. Furuya, *J. Mater. Sci.* **2006**, *41*, 4532.
- [16] A. Fernández-Pacheco, L. Serrano-Ramón, J. M. Michalik, M. R. Ibarra, J. M. De Teresa, L. O'Brien, D. Petit, J. Lee, R. P. Cowburn, *Sci. Rep.* **2013**, *3*, 1492.
- [17] P. Vavassori, V. Metlushko, B. Ilic, M. Gobbi, M. Donolato, M. Cantoni, R. Bertacco, *Appl. Phys. Lett.* **2008**, *93*, 203502.
- [18] M. Donolato, M. Gobbi, P. Vavassori, M. Leone, M. Cantoni, V. Metlushko, B. Ilic, M. Zhang, S. X. Wang, R. Bertacco, *Nanotechnology* **2009**, *20*, 385501.

- [19] M. T. Bryan, J. Dean, T. Schrefl, F. E. Thompson, J. Haycock, D. A. Allwood, *Appl. Phys. Lett.* **2010**, *96*, 192503.
- [20] E. Rapoport, D. Montana, G. S. D. Beach, *Lab Chip* **2012**, *12*, 4433.
- [21] R. Lavrijsen, R. Córdoba, F. J. Schoenaker, T. H. Ellis, B. Barcones, J. T. Kohlhepp, H. J. M. Swagten, B. Koopmans, J. M. De Teresa, C. Magén, M. R. Ibarra, P. Trompenaars, J. J. L. Mulders, *Nanotechnology* **2011**, *22*, 025302.
- [22] R. Córdoba, R. Lavrijsen, A. Fernández-Pacheco, M. R. Ibarra, F. Schoenaker, T. Ellis, B. Barcones-Campo, J. T. Kohlhepp, H. J. M. Swagten, B. Koopmans, J. J. L. Mulders, J. M. De Teresa, *J. Phys. D. Appl. Phys.* **2012**, *45*, 035001.
- [23] C. W. Sandweg, N. Wiese, D. McGrouther, S. J. Hermsdoerfer, H. Schultheiss, B. Leven, S. McVitie, B. Hillebrands, J. N. Chapman, *J. Appl. Phys.* **2008**, *103*, 093906.
- [24] J. Chapman, *J. Phys. D. Appl. Phys.* **1984**, *17*, 623.
- [25] P. J. Metaxas, P.-J. Zermatten, J.-P. Jamet, J. Ferré, G. Gaudin, B. Rodmacq, A. Schuhl, R. L. Stamps, *Appl. Phys. Lett.* **2009**, *94*, 132504.
- [26] L. O'Brien, D. Petit, E. Lewis, R. Cowburn, D. Read, J. Sampaio, H. Zeng, A.-V. Jausovec, *Phys. Rev. Lett.* **2011**, *106*, 087204.
- [27] V. L. Mironov, O. L. Ermolaeva, E. V. Skorohodov, A. Y. Klimov, *Phys. Rev. B* **2012**, *85*, 144418.
- [28] S.-M. Ahn, K.-W. Moon, C.-G. Cho, S.-B. Choe, *Nanotechnology* **2011**, *22*, 085201.
- [29] M. Vázquez, G. Basheed, G. Infante, R. Del Real, *Phys. Rev. Lett.* **2012**, *108*, 037201.
- [30] L. O'Brien, A. Beguivin, A. Fernandez-Pacheco, D. Petit, D. E. Read, R. P. Cowburn, *Appl. Phys. Lett.* **2012**, *101*, 062415.
- [31] R. Lavrijsen, J. H. Franken, J. T. Kohlhepp, H. J. M. Swagten, B. Koopmans, *Appl. Phys. Lett.* **2010**, *96*, 222502.
- [32] J. H. Franken, M. Hoeijmakers, R. Lavrijsen, J. T. Kohlhepp, H. J. M. Swagten, B. Koopmans, E. van Veldhoven, D. J. Maas, *J. Appl. Phys.* **2011**, *109*, 07D504.
- [33] J. H. Franken, M. Hoeijmakers, R. Lavrijsen, H. J. M. Swagten, *J. Phys. Cond. Matter* **2012**, *24*, 024216.
- [34] M. R. Scheinfein, LLG micromagnetics simulator.
- [35] M. Cyrot, E. de Lacheisserie, *Magnetism: Fundamentals*; Springer, 2007.
- [36] R. I. Joseph, *J. Appl. Phys.* **1966**, *37*, 4639.
- [37] H.-B. Braun, *Phys. Rev. Lett.* **1993**, *71*, 3557.

- [38] S. X. Wang, G. Li, *IEEE Trans. Magn.* **2008**, *44*, 1687.
- [39] D. L. Graham, H. A. Ferreira, P. P. Freitas, *Trends Biotechnol.* **2004**, *22*, 455.
- [40] M. Donolato, P. Vavassori, M. Gobbi, M. Deryabina, M. F. Hansen, V. Metlushko, B. Ilic, M. Cantoni, D. Petti, S. Brivio, R. Bertacco, *Adv. Mater.* **2010**, *22*, 2706.
- [41] E. Rapoport, G. S. D. Beach, *Appl. Phys. Lett.* **2012**, *100*, 082401.
- [42] A. Ehresmann, D. Lengemann, T. Weis, A. Albrecht, J. Langfahl-Klabes, F. Göllner, D. Engel, *Adv. Mater.* **2011**, *23*, 5568.
- [43] N. Kikuchi, S. Okamoto, O. Kitakami, Y. Shimada, K. Fukamichi, *Appl. Phys. Lett.* **2003**, *82*, 4313.

Table of contents entry

Vertical magnetic nanopillars grown by electron-beam induced deposition are used to control pinning of magnetic domain walls, moving through an underlying conduit. The pinning strength depends on the height and magnetic state of the pillars, and this is used to determine the switching field of the pillars themselves.

Nanomagnetism

J.H. Franken, M.A.J. van der Heijden, T. Ellis, R. Lavrijsen, C. Daniels, D. McGrouther, H.J.M. Swagten*, and B. Koopmans

Beam-induced Fe nanopillars as tunable domain-wall pinning sites

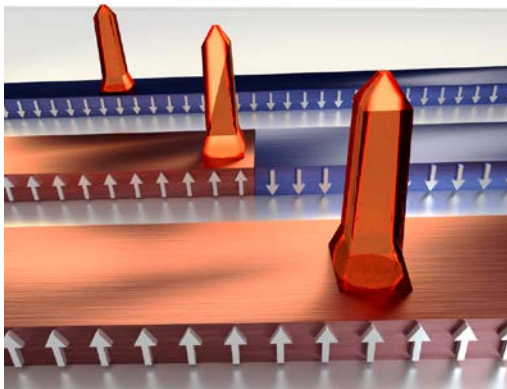


(Image provided by Matthijs Cox)

Supporting Information

1. Stray field calculation

As known from elementary electromagnetism, a magnetized object generates bound currents. A simple way to calculate the stray fields of such an object is to find the magnetic field generated by those currents. In a uniformly magnetized pillar, the bound volume current $\vec{J}_b = \nabla \times \vec{M}$ vanishes, but there remains a bound surface current $\vec{K}_b = \vec{M} \times \hat{n} = M_s \hat{\phi}$. So, a total current of $M_s \cdot h$ flows over the curved cylinder surface, with h the cylinder height. We calculate the field produced by this current by dividing the cylinder into N tiny slices, each of which is a current loop with $I = \frac{M_s \cdot h}{N}$. Starting from the Biot-Savart law, the following expression can be derived for the position-dependent r and z components of the magnetic field produced by a single current loop of radius a ^[1],

$$H_r(r, z) = H_0 \frac{\gamma}{\pi \sqrt{Q}} \left(E(k^2) \frac{1 + \alpha^2 + \beta^2}{Q - 4\alpha} - K(k^2) \right), \quad (\text{S1})$$

$$H_z(r, z) = H_0 \frac{1}{\pi \sqrt{Q}} \left(E(k^2) \frac{1 - \alpha^2 - \beta^2}{Q - 4\alpha} + K(k^2) \right), \quad (\text{S2})$$

where $\alpha = \frac{r}{a}$, $\beta = \frac{z}{a}$, $\gamma = \frac{z}{r}$, $Q = (1 + \alpha)^2 + \beta^2$, $k^2 = \frac{4ar}{(a+r)^2 + z^2}$, and $H_0 = \frac{I}{2a}$ (the field in the center of the loop). $K(k^2)$ and $E(k^2)$ furthermore represent the complete elliptical integrals of the first and second kind,

$$K(k^2) = \int_{\vartheta=0}^{\frac{\pi}{2}} \frac{d\vartheta}{\sqrt{1 - k^2 \sin^2 \vartheta}}, \quad (\text{S3})$$

$$E(k^2) = \int_{\vartheta=0}^{\frac{\pi}{2}} \sqrt{1 - k^2 \sin^2 \vartheta} d\vartheta. \quad (\text{S4})$$

We used a MATLAB script to calculate the field produced by a superposition of N loops. As a simplification, we assume that the domain wall (DW) only senses the z -component of the field, which is, in principle, valid if the DW is very small. We calculate the field in the plane $d = 2$ nm (the thickness of our Pt cap layer) below the first loop, by summing Eq. (S2) over all N loops,

$$H_{z,\text{tot}} = \sum_{i=1}^N H_z(r, -d - \frac{h}{N}(i + \frac{1}{2})). \quad (\text{S5})$$

Figure S1 shows 2D plots of H_z for two different pillar heights, magnetized in the $-z$ direction. We choose $M_s = 100$ kA/m, the pillar radius $a = 30$ nm, and divided the pillar into $N = 50$ slices. Comparing Figure S1(a) and (b), it is observed that the smaller pillar produces higher stray fields in a ring around the pillar (white area around the pillar), whereas the taller pillar has higher (negative) stray fields right underneath the pillar (darker black dot in the center). However, this does not directly gives us the minimum and maximum field experienced by the

DW as a whole. If we assume a 1D profile of the DW that varies only in the x -direction, the DW feels the field strength averaged over its length, which is along the entire width of the strip (500 nm) spanning the y -axis. The average z -field as a function of DW position x is plotted in Figure 1(c) and (d). The extrema in plots 1(c) and (d) directly give us the pinning and pulling field as defined in the main text. The results of these calculations as a function of pillar height are shown in Figure 3(b) in the main text.

As discussed, the limitation of this model is the fact that the DW does not fully retain its 1-dimensional character, and the in-plane stray fields also play a role since the DW has finite width. This is exactly what was taken into account in the full micromagnetic simulations in Figure 3(b) in the main text, which give slightly different results.

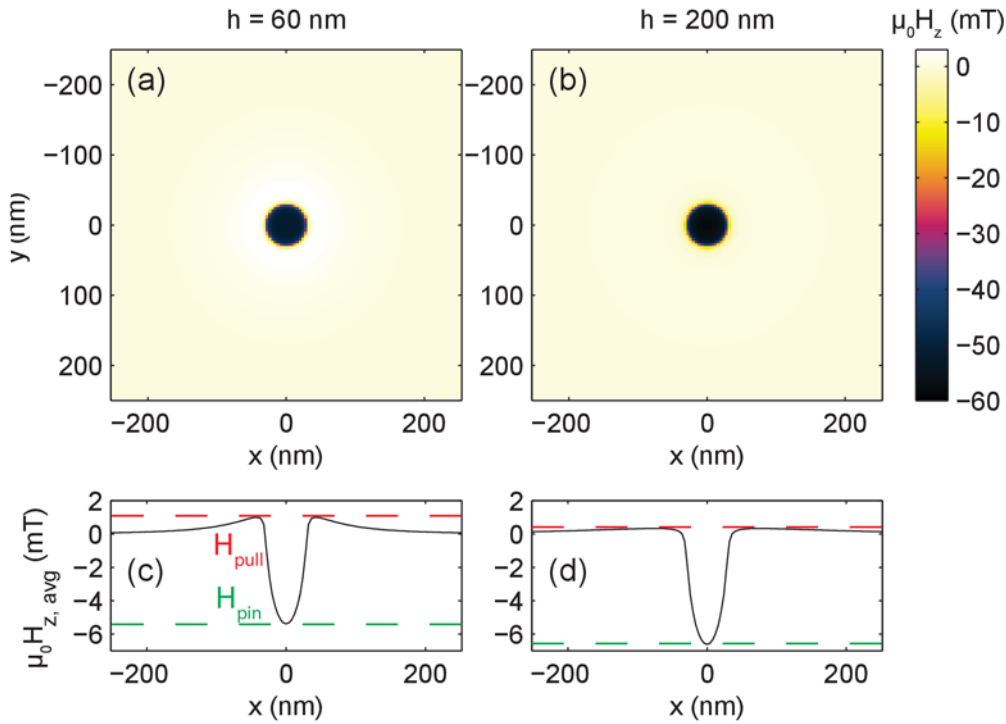


Figure S1. Calculated z -stray fields of pillars with height 60 nm (a) and 200 nm (b). (c) and (d) show the same data averaged over the y -direction. The minimum and maximum are defined as H_{pin} and H_{pull} , respectively.

2. Coercive field calculation

Here, we derive an expression for the coercive field of a pillar in a Stoner-Wohlfarth model, assuming that the magnetization in the pillar remains uniform during switching. The two energy terms that play a role are the Zeeman energy due to the interaction of the magnetization with the externally applied magnetic field H_{ext} , and the shape anisotropy K_s that the pillar exhibits because it is elongated in the z -direction. Hence, the total energy density of the system can be written as

$$U = K_s \sin^2 \theta - \mu_0 M_s H_{\text{ext}} \cos(\phi - \theta), \quad (\text{S6})$$

where θ is the angle of the magnetization vector and ϕ the angle of the externally applied field, both with respect to the z -axis. Like in the experiment, the external field is applied in the z direction, so $\phi = 0$. According to the Stoner-Wohlfarth theory, the magnetization direction of a magnetized object reverses upon a sign reversal of the second derivative of the total

energy U with respect to θ . Because of symmetry considerations, any angle other than $\theta = 0$ or π is unstable, hence $\theta = 0$ at the moment the switch occurs. Hence, the switching condition reads

$$\left. \frac{\partial^2 U}{\partial \theta^2} \right|_{\theta=0} = 2K + \mu_0 M_s H_{\text{ext}} = 0, \quad (\text{S7})$$

yielding

$$\mu_0 H_{\text{ext}} = \frac{-2K}{M_s}. \quad (\text{S8})$$

The remaining task is to find an expression for the shape anisotropy constant K_s . For simple shapes like ellipsoids, the shape anisotropy of a magnetized object scales with the difference between the demagnetizing factors along the easy and hard axis, or more explicitly^[2]:

$$K_s = \frac{\mu_0 M_s^2}{2} (N_x - N_z) = \frac{\mu_0 M_s^2}{4} (1 - 3N_z), \quad (\text{S9})$$

where N_x and N_z represent the demagnetizing factors in respectively the x (hard axis) and z (easy axis) direction. Note that also $N_x + N_y + N_z = 1$ and $N_x = N_y$ have been used to rewrite the expression. To calculate N_z , we use the expression for the magnetometric demagnetizing factor of a uniformly magnetized cylinder from^[3]:

$$N_z = 1 - \frac{2}{2\pi p} \left\{ (1 + p^2)^{\frac{1}{2}} \times [p^2 K(k) + (1 - p^2)E(k)] - 1 \right\}, \quad (\text{S10})$$

with $k = (1 + p^2)^{-1}$ and $p = \frac{h}{2a}$ the aspect ratio of the pillar. $K(k)$ and $E(k)$ again represent the complete elliptic integrals of the first and second kind defined in (S3) and (S4).

Finally, to find values for the coercive field of a pillar, we combine equations (S8), (S9) and (S10). The coercive field as a function of pillar aspect ratio p is shown in Figure 4(b) in the main text (grey dashed line).

Supplementary references

- [1] D. B. Montgomery, J. Terrell, *Air Force Contract AF* **1961**, *19*, 7344.
- [2] M. Cyrot, E. de Lacheisserie, *Magnetism: Fundamentals*; Springer, 2007.
- [3] R. I. Joseph, *J. Appl. Phys.* **1966**, *37*, 4639.